

Supporting Information for

Embedding Ultrafine Metal Oxide Nanoparticles in Monolayered Metal-Organic Framework Nanosheets Enables Efficient Electrocatalytic Oxygen Evolution

Wang Zhang,^{†,¶,‡} Yu Wang,^{†,‡} Han Zheng,[†] Rui Li,[#] Yujia Tang,[#] Boyuan Li,[#] Chao Zhu,[§]

Liming, You,[†] Min-Rui Gao,[‡] Zheng Liu,[§] Shu-Hong Yu,[‡] and Kun Zhou^{†,*}

[†]Environmental Process Modelling Centre, Nanyang Environment and Water Research Institute, Nanyang Technological University, 1 Cleantech Loop, Singapore 637141, Singapore.

[¶]School of Materials Science and Engineering, Zhejiang University of Technology, 18 Chaowang Road, Hangzhou, Zhejiang 310014, P.R.China.

[#]School of Mechanical and Aerospace Engineering, Nanyang Technological University, 50 Nanyang Avenue, Singapore 639798, Singapore.

[§]School of Materials Science and Engineering, Nanyang Technological University, 50 Nanyang Avenue, Singapore 639798, Singapore.

[‡]Hefei National Laboratory for Physical Sciences at the Microscale, University of Science and Technology of China, 96 Jinzhai Road, Hefei, Anhui 230026, P. R. China.

[‡]These authors contributed equally to this work.

*Corresponding author e-mail: kzhou@ntu.edu.sg

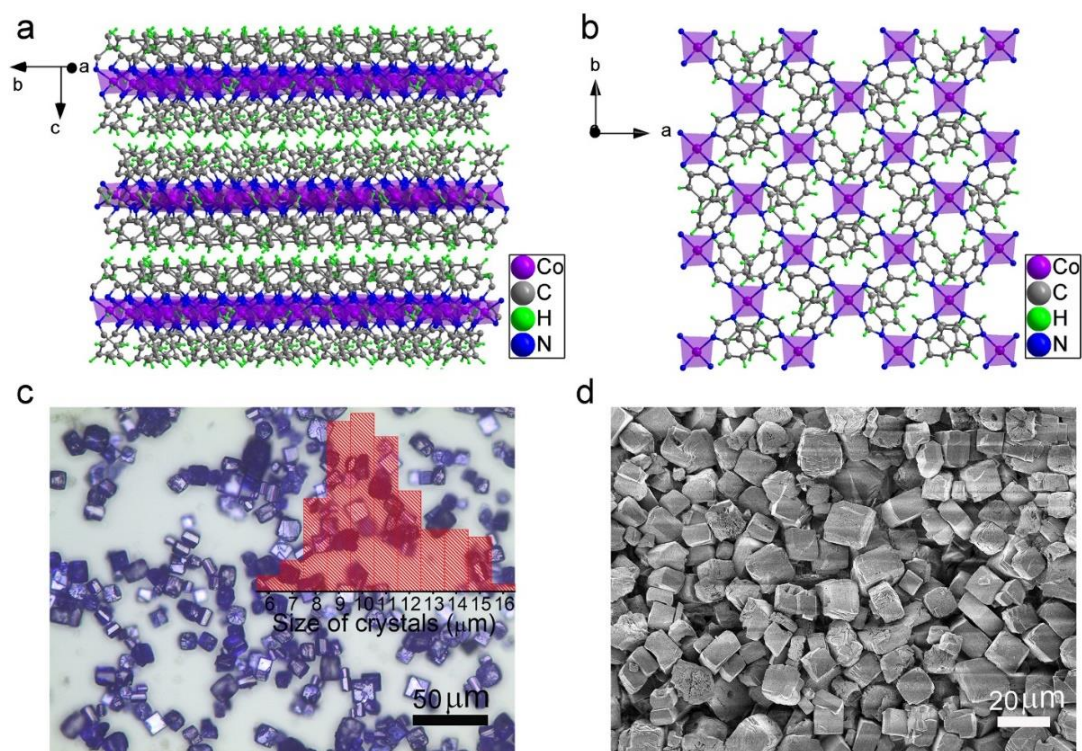


Figure S1. Crystalline architecture (a) and layered structure (b) illustration, optical microscopy (c) and FE-SEM (d) images of PCB. Purple tetrahedral geometry represents the CoN₄ secondary unit structure. Inset in (c) shows the corresponding PCB crystal size distribution in term of the statistics of 120 samples.

In the PCB structure, each Co atom is four-coordinated by benzimidazole linkers while each linker bridges two Co atoms. The CoN₄ secondary unit structures connected by benzimidazole linkers make up infinite two-dimensional (2D) sheets interacted by van der Waals forces.

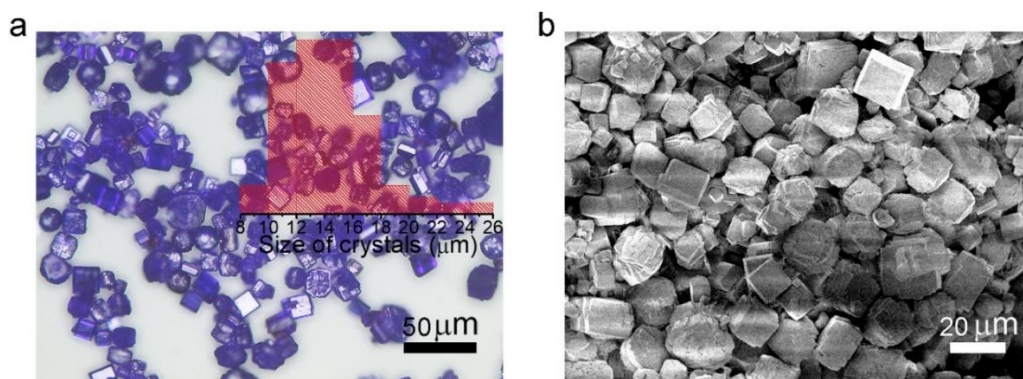


Figure S2. Optical microscopy (a) and FE-SEM (b) images of M-PCB. Inset in (a) shows the corresponding M-PCB crystal size distribution in term of the statistics of 120 samples.

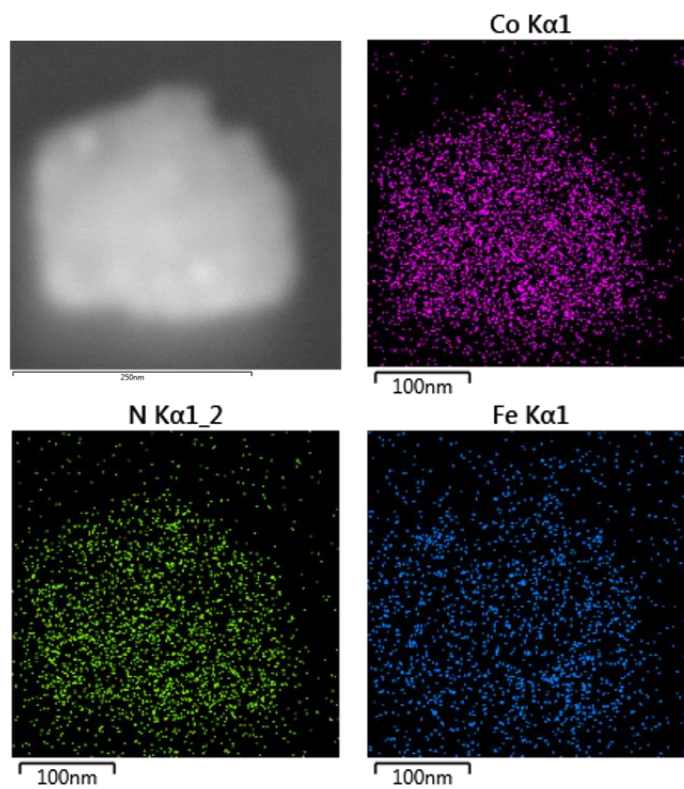


Figure S3. STEM image and the corresponding element mapping of M-PCB.

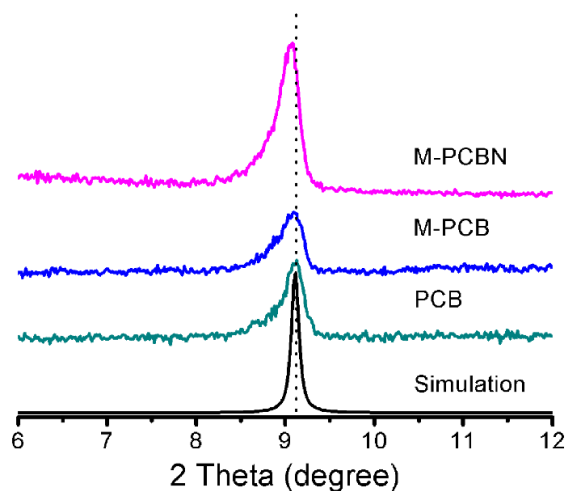


Figure S4. Magnifying PXRD patterns from 6° to 12° of PCB, M-PCB and M-PCBN, as well as the simulated diffraction pattern.

The diffraction peak at 9.1° is assigned to the (002) plane, which is shown in M-PCBN due to the restacking of nanosheets during the preparation process for PXRD measurement.

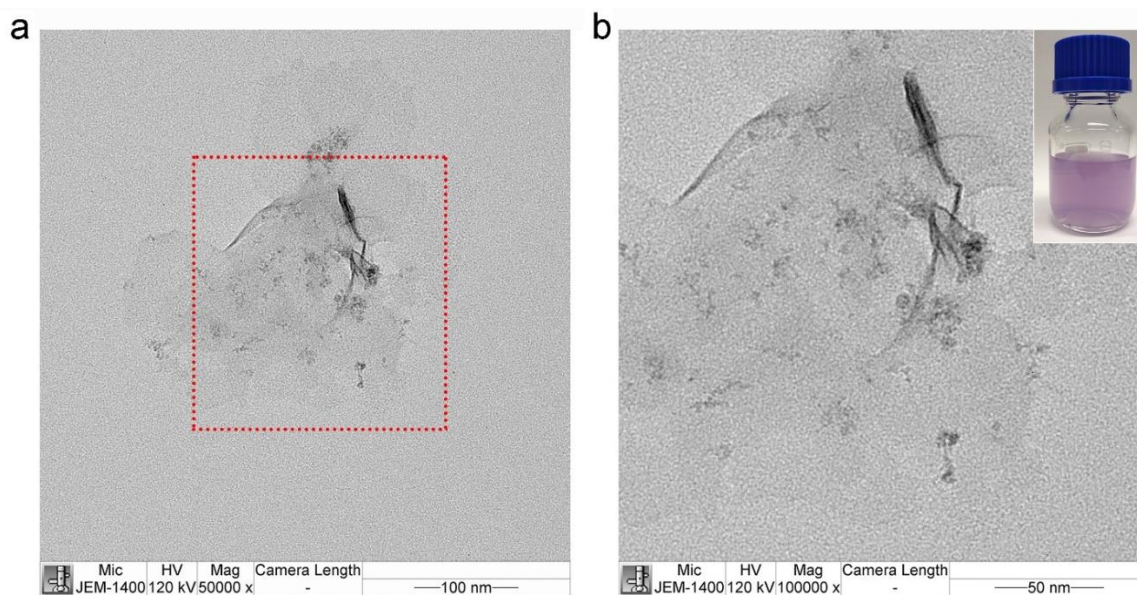


Figure S5. TEM images of a piece of M-PCBN. (b) shows the magnification TEM image of the red rectangle area in (a). Inset of (b) shows the photograph of M-PCBN in an organic solvent for more than four months.

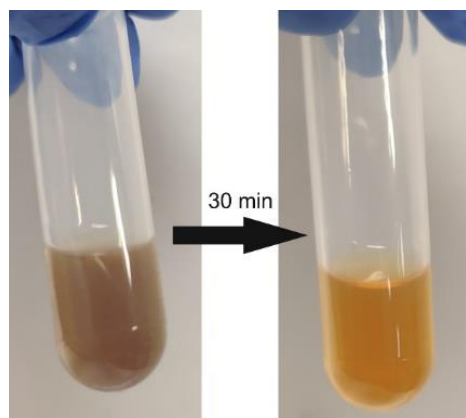


Figure S6. Demonstration experiment for the structural deterioration of PCB microcrystals under Fe^{3+} solution.

4 mg of PCB was dispersed into 2 mL of iron (III) nitrate nonahydrate methanol solution (10 mmol L^{-1}). The mixed solution became clear after 30 min, indicating that PCB microcrystals were completely decomposed.

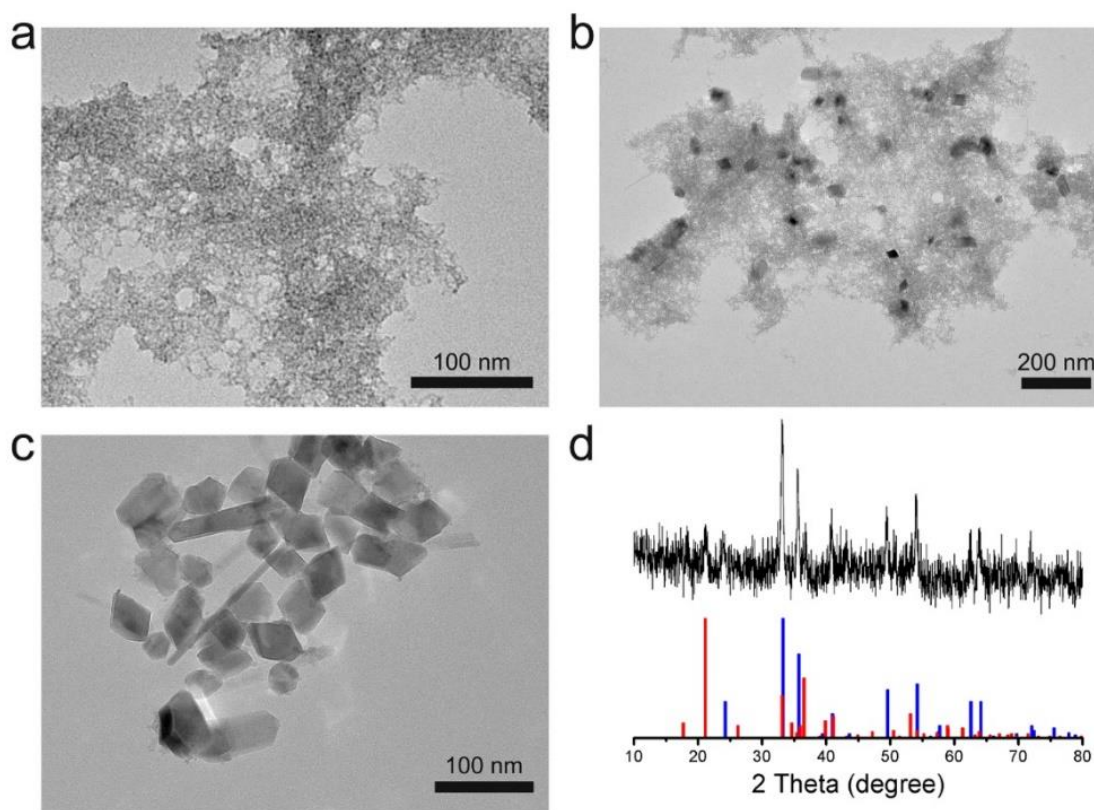


Figure S7. TEM images of Fe-benzimidazole (a) and products obtained in control experiments at 80 °C (b) and 110 °C (c). (d) Powder XRD pattern of the product obtained in a control experiment at 110 °C and the standard hematite (blue, JCPDS No. 33-0664) and goethite (red, JCPDS No. 29-0713) patterns.

In the synthesis process of M-PCB, most Fe^{3+} ions coordinated with benzimidazole to form an amorphous oligomer as shown in (a). The Fe-benzimidazole oligomer can be removed by washing with methanol under ultrasonication.

In the control experiments, the products obtained at 80 °C contain the Fe-benzimidazole oligomer and inorganic nanoparticles as shown in (b). By further increasing the reactive temperature to 110 °C, inorganic nanoparticles as shown in (c) can be observed with the oligomer disappeared. The crystalline structure of these nanoparticles was confirmed by the powder XRD pattern (d), suggesting the presence of two Fe-based oxide phases including hematite and goethite.

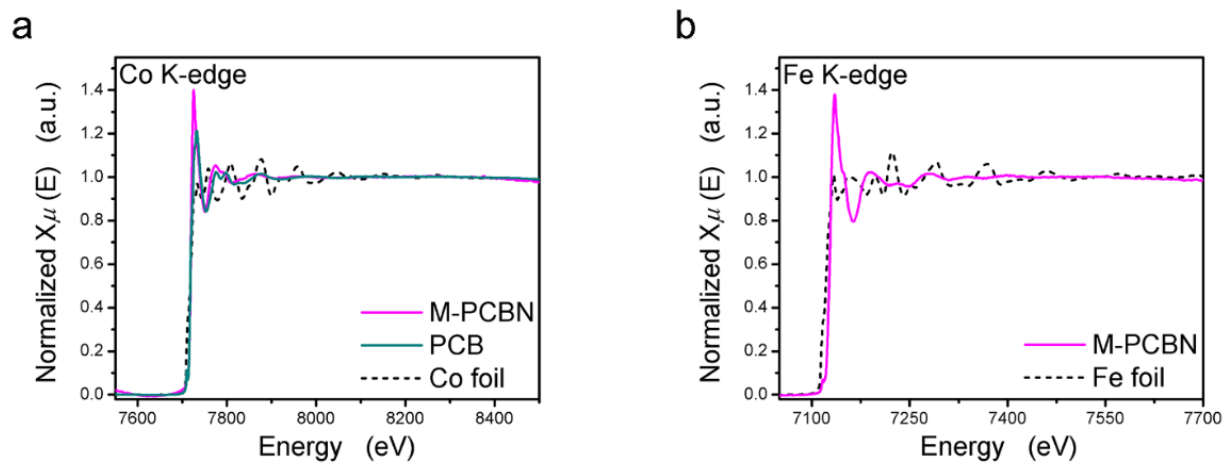


Figure S8. Normalized Co K-edge (a) and Fe K-edge (b) XAS spectra for PCB, M-PCBN and standard metal foils.

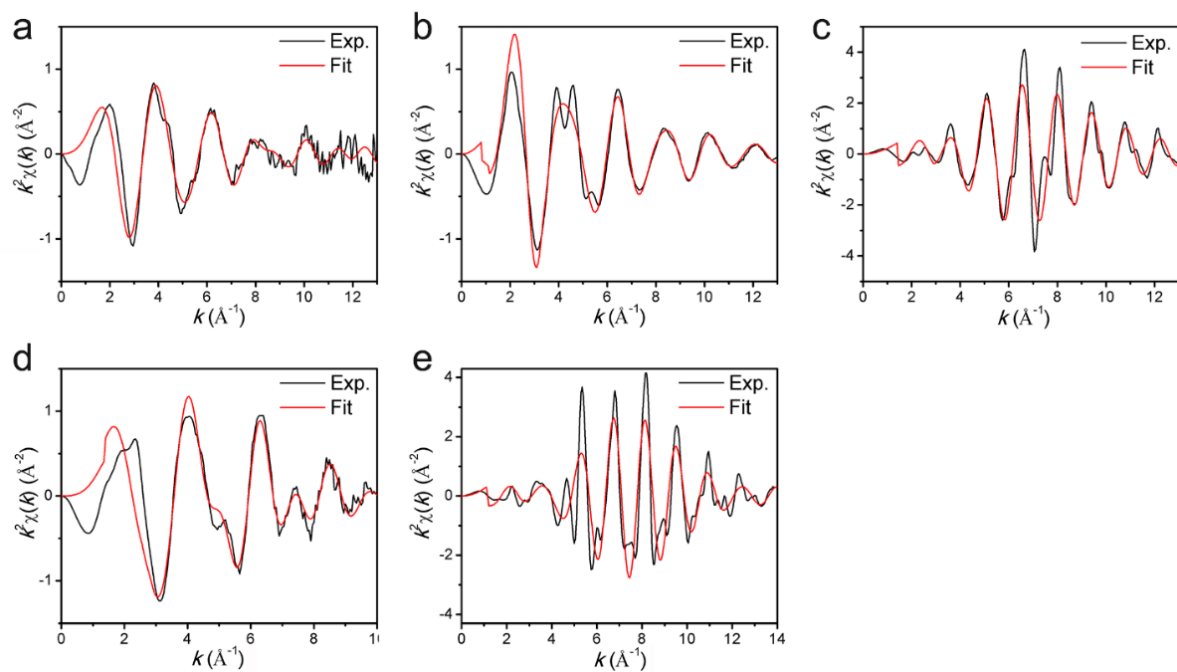


Figure S9. k^2 -weighted spectra in k space for PCB, M-PCBN and standard metal foils. Co K-edge spectra for PCB (a), M-PCBN (b) and Co foil (c); Fe K-edge spectra for M-PCBN (d) and Fe foil (e).

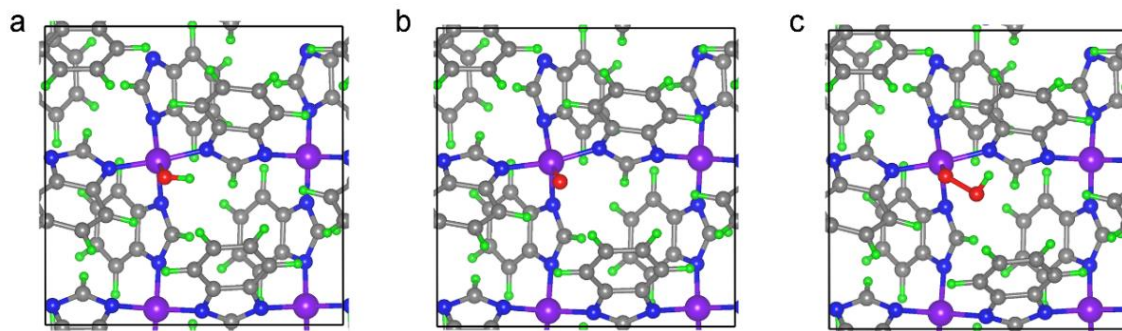


Figure S10. Top views of OER intermediates: OH* (a), O* (b), and OOH* (c) on p-CoN₄.

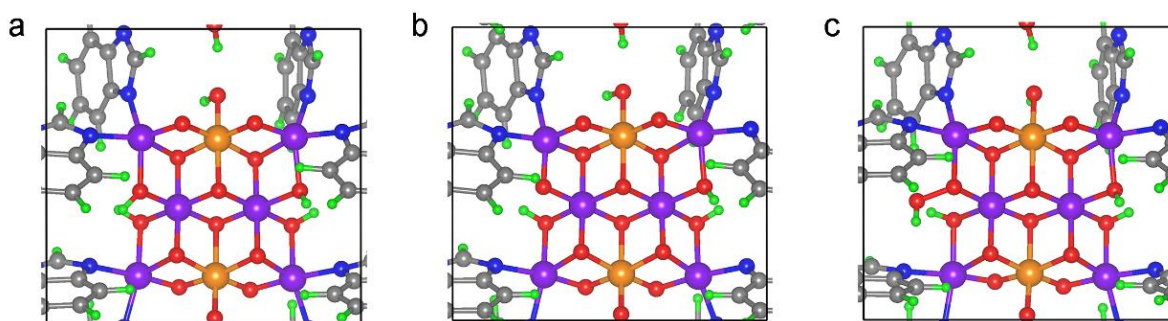


Figure S11. Top views of OER intermediates: OH* (a), O* (b), and OOH* (c) on i-Co-Co. Geometric structures of intermediates for i-Co-Fe are same with those for i-Co-Co.

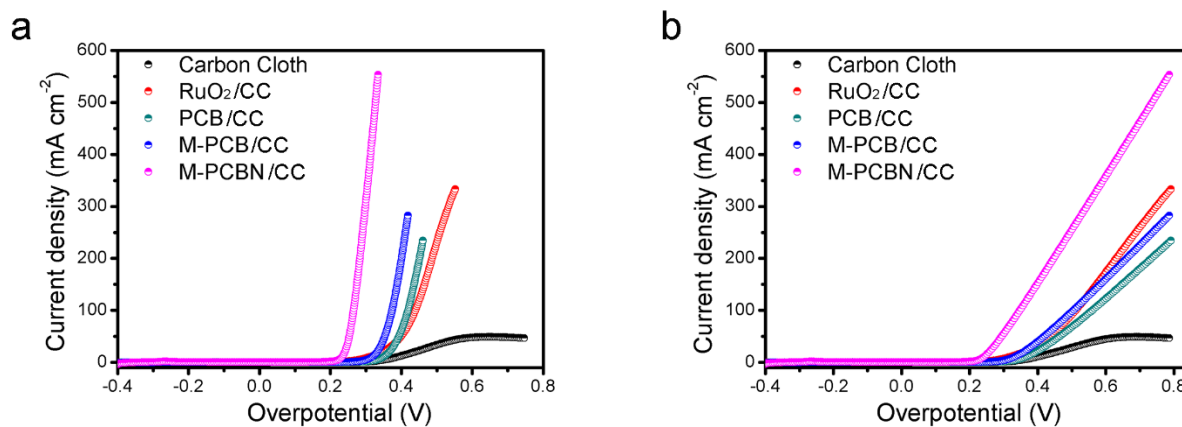


Figure S12. Polarization curves for all working electrodes with (a) and without (b) 95%*iR* correction measured under an O₂-saturated 1 M KOH electrolyte and recorded at a scan rate of 5 mV s⁻¹.

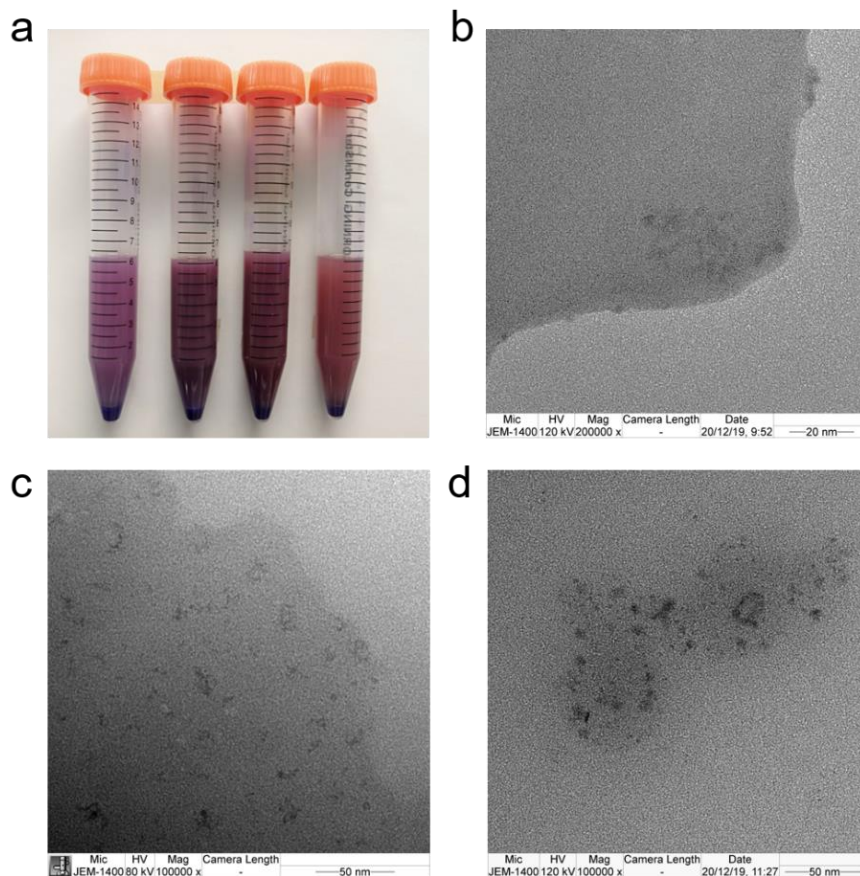


Figure S13. (a) Photographs of S-10, S-20, S-30 and S-40 (from left to right) after ultrasonication. TEM images: (b) S-10, (c) S-30 and (d) S-40.

The exfoliated samples are labeled as S-10, S-20 (M-PCBN in the main text), S-30 and S-40, which correspond to the different molar ratio of feeds at 10% (1 mM), 20% (2 mM), 30% (3 mM) and 40% (4 mM) of $\text{Fe}(\text{NO}_3)_3 \cdot 9\text{H}_2\text{O}$ with a constant concentration of $\text{Co}(\text{NO}_3)_2 \cdot 6\text{H}_2\text{O}$ (10 mM) in the synthesis steps. Figure S13a shows the photographs of products after exfoliation. The exfoliation rates of S-10, S-20 (M-PCBN), S-30 and S-40 were $\sim 9.1\%$, $\sim 25\%$, $\sim 17.5\%$ and $\sim 3.2\%$, respectively. Because trivalent Fe ions can attack the CoN_4 -based MOF structure, excess Fe ions lead to a decreased exfoliation rate during the ultrasonic process. The Fe content in S-10, S-20 (M-PCBN), S-30 and S-40 were calculated to be 2.21 wt%, 4.14 wt%, 5.33 wt% and 6.89 wt%, respectively, by ICP-OES. When the less concentrated Fe precursor was used, the TEM image of S-10 shows that insufficient metal oxide nanoparticles are embedded on the MOF matrix (Figure S13b). By increasing the concentration of the Fe precursor, the TEM image of S-30 shows similar results with S-20 (M-PCBN) (Figure S13c). When an excessively concentrated Fe precursor was added, the size of metal oxide nanoparticles increased and the yield of resultant product declined (Figure S13d).

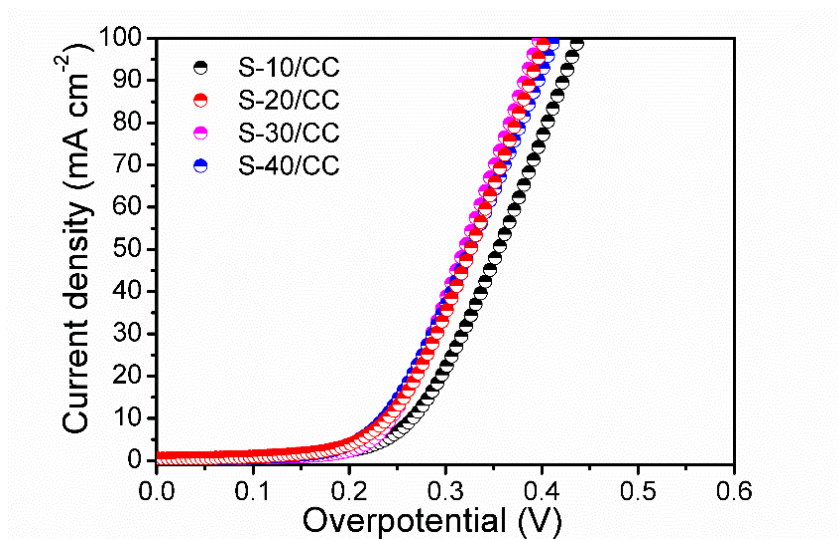


Figure S14. Polarization curves for S-10/CC, S-20/CC (M-PCBN/CC), S-30/CC and S-40/CC without iR correction measured under the 1 M KOH electrolyte and recorded at a scan rate of 5 mV s^{-1} .

S-10/CC exhibits the highest overpotential of 266 mV at a current density of 10 mA cm^{-2} , while the others achieve similar results with overpotentials around 240 mV at 10 mA cm^{-2} . When the low concentration of Fe precursor is used, the formed metal oxide nanoparticles and created active interfaces are insufficient in the resultant S-10 and thus its OER activity is lower than the others. On the contrary, S-30/CC and S-40/CC exhibit nearly identical polarization curves with S-20/CC (M-PCBN/CC), confirming that the active interface is saturated when the molar ratio of the Fe precursor exceeds 20% and the Fe sites in the metal oxide are inactive.

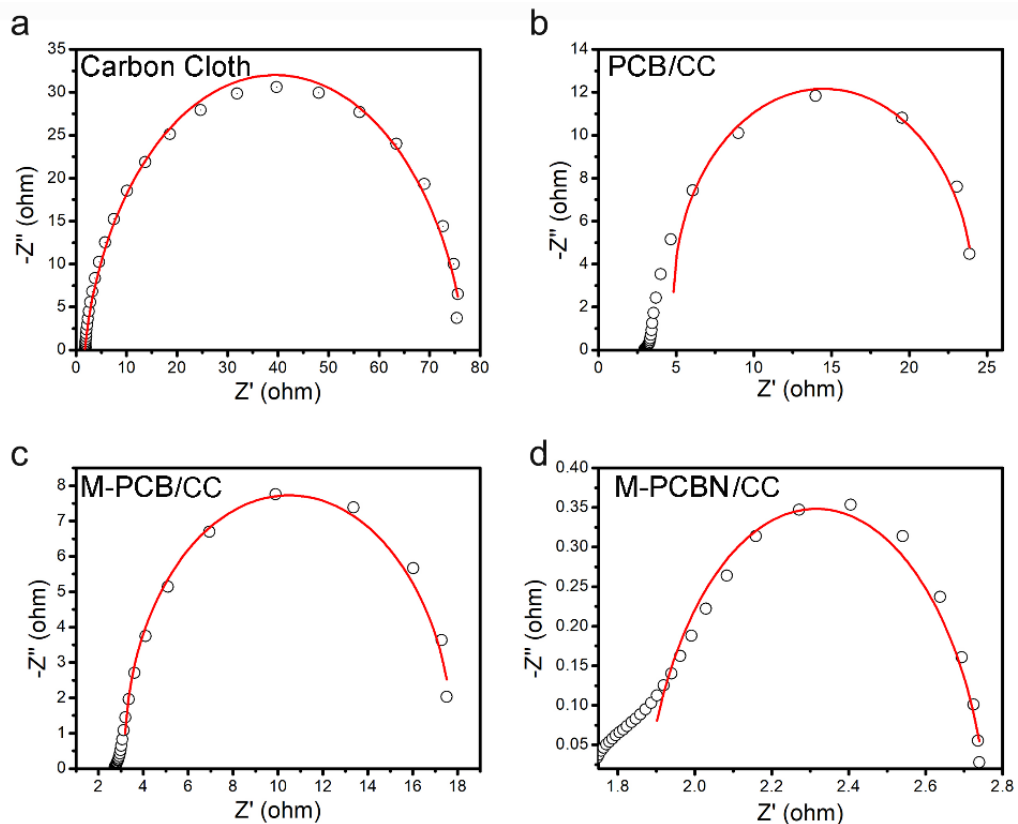


Figure S15. EIS for pristine carbon cloth (a), PCB/CC (b), M-PCB/CC (c) and M-PCBN/CC (d).

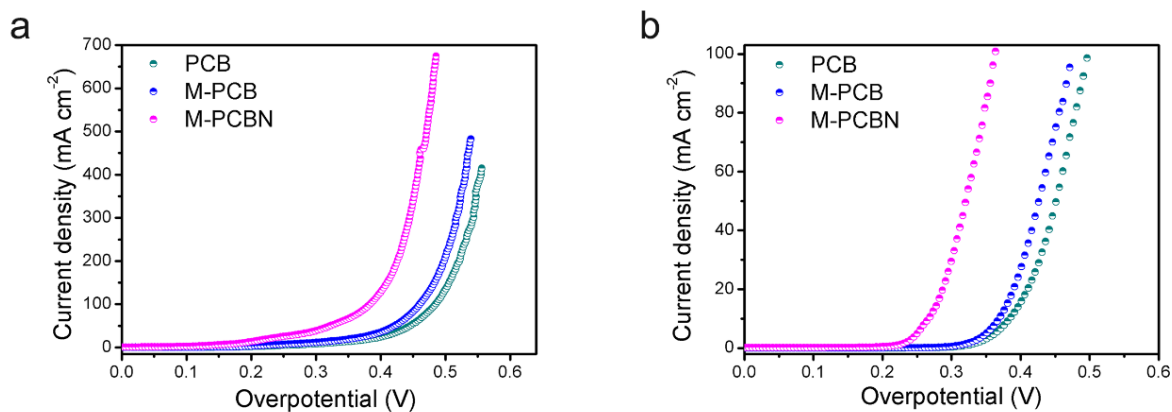


Figure S16. Polarization curves for PCB, M-PCB and M-PCBN deposited on copper foam (a) and glassy carbon electrode (b) with 95% iR correction measured under an O_2 -saturated 1 M KOH electrolyte and recorded at a scan rate of 5 mV s^{-1} .

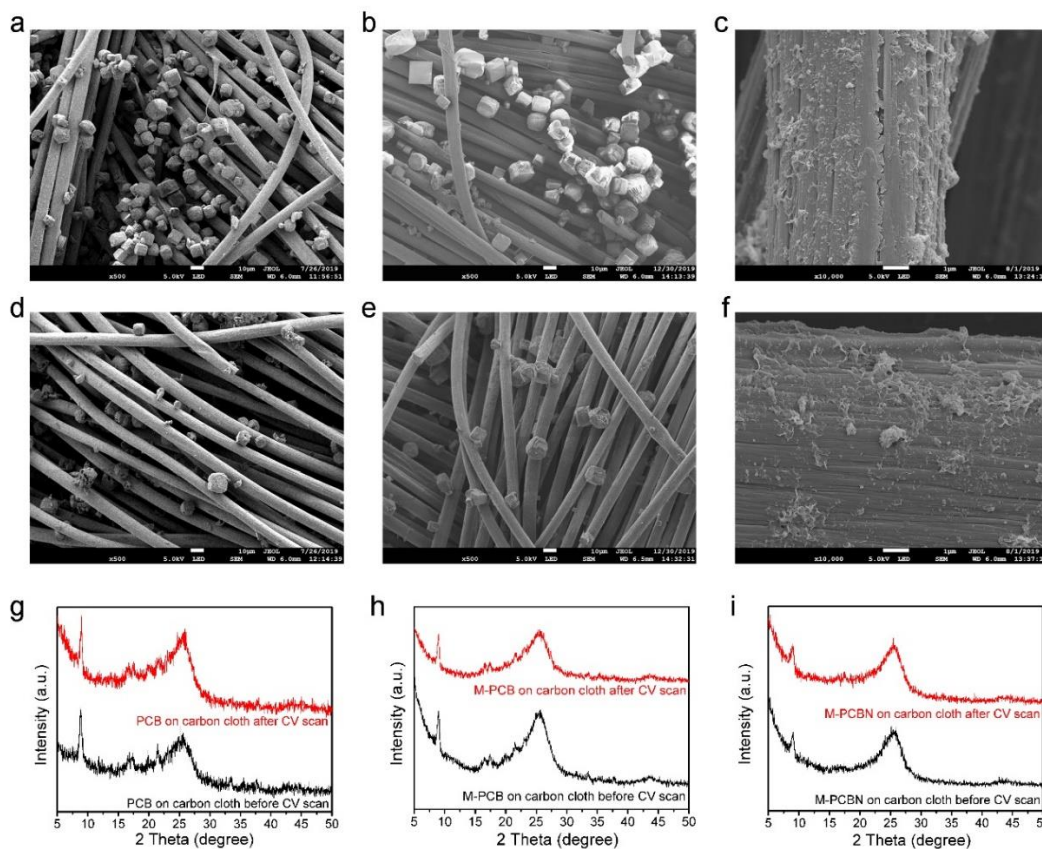


Figure S17. SEM images of PCB (a,d), M-PCB (b,e) and M-PCBN (c,f) deposited on carbon cloth before (a-c) and after (d-f) the CV cycle test. XRD patterns of PCB (g), M-PCB (h), and M-PCBN (i) deposited on carbon cloth before and after the CV cycle test.

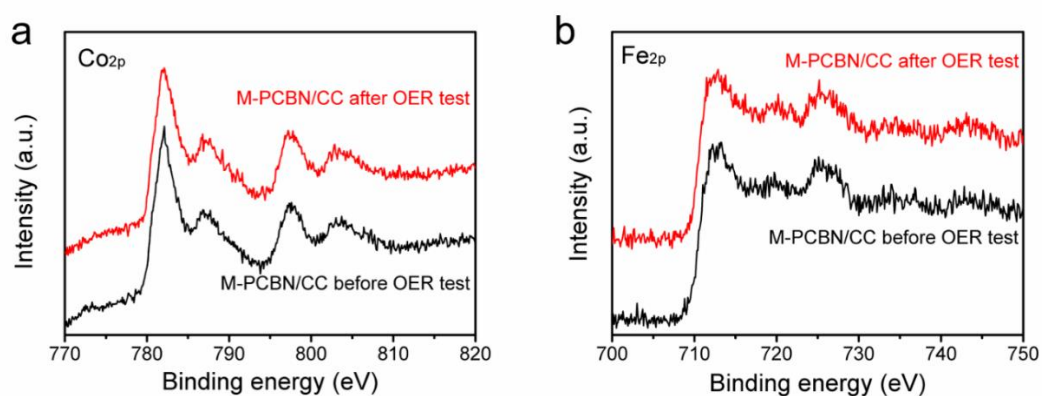


Figure S18. High-resolution XPS spectra for M-PCBN/CC before and after the electrochemical OER test: (a) Co_{2p} and (b) Fe_{2p}.

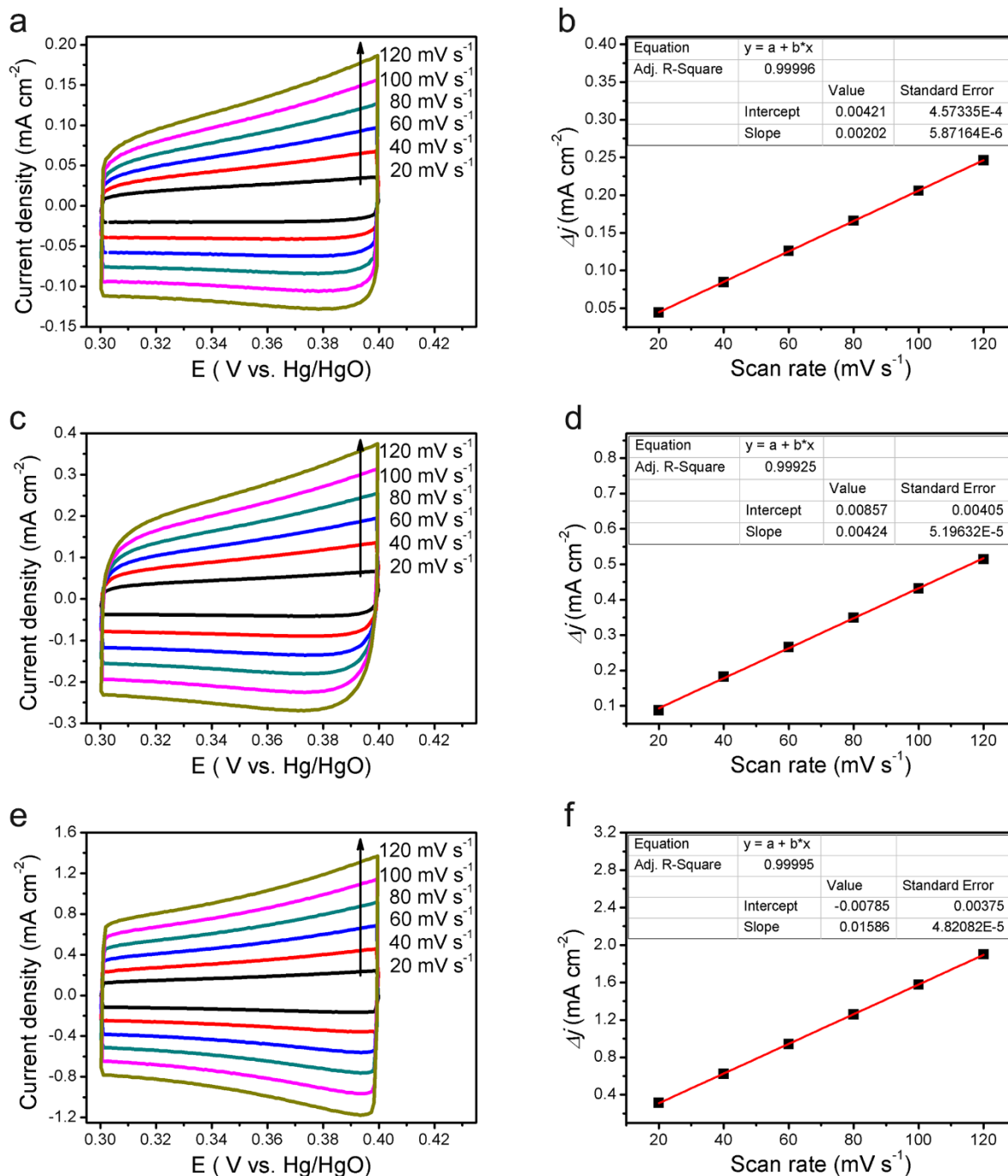


Figure S19. Cyclic voltammetry (CV) curves for PCB (a), M-PCB (c) and M-PCBN (e) deposited on a glassy carbon electrode and measured in a potential window of 0.3-0.4 V (versus Hg/HgO) with different scan rates from 20 to 120 mV s^{-1} . The corresponding linear relation of the charging current density differences at 0.35 V (versus Hg/HgO) against scan rates for PCB (b), M-PCB (d) and M-PCBN (f).

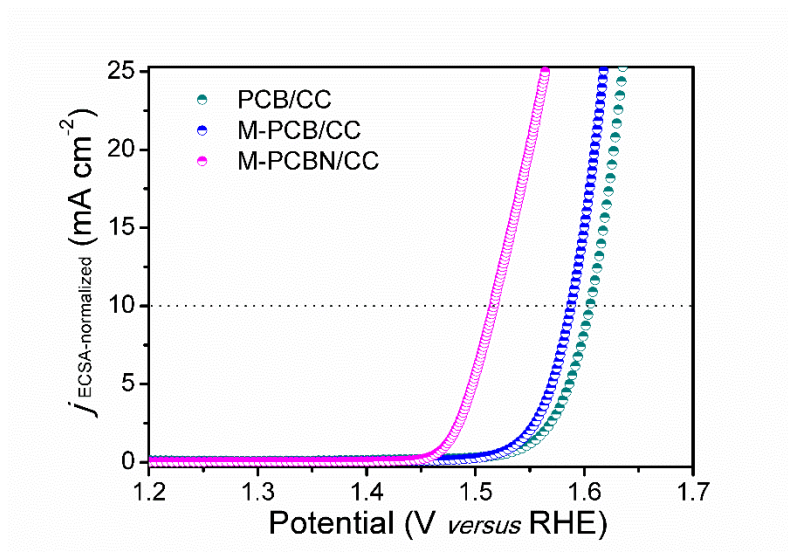


Figure S20. Polarization curves normalized by ECSA for PCB/CC, M-PCB/CC and M-PCBN/CC.

Table S1. Fitting parameters of EXAFS curve for PCB, M-PCBN, Co and Fe foils.

Sample	Path	C.N.	R (Å)	$\sigma^2 \times 10^3$ (Å ²)	ΔE (eV)	R factor
Co foil	Co-Co	12 ^a	2.50±0.01	6.3±0.2	8.0±0.3	0.001
M-PCBN	Co-N/O	3.4±0.5	2.01±0.01	7.4±2.0	-1.4±1.6	0.013
	Co-C	2.7±1.3	2.97±0.05	7.9±6.9	3.0±3.6	
PCB	Co-N	4.3±0.3	2.00±0.01	4.5±0.6	4.9±0.8	0.002
	Co-C	6.9±1.5	2.95±0.02	9.7±2.6	2.7±1.5	
Fe foil	Fe-Fe	8 ^a	2.46±0.01	4.8±1.4	5.4±2.2	0.004
	Fe-Fe	6 ^a	2.84±0.02	5.6±2.5	4.6±3.6	
M-PCBN ^b	Fe-O	5.7±0.7	1.96±0.01	11.0±1.8	-5.2±1.8	0.005
	Fe-Fe/Co	4.6±1.3	3.09±0.02	12.8±3.1	7.2±2.4	

^aThe coordination number (C.N.) is fixed according to the corresponding crystal data.

^bThe fitting results show the inexistence of an Fe-N coordination mode.

Table S2. Comparison of electrocatalytic activity of the recent electrocatalysts for OER.

Electrocatalysts	Electrolyte	Substrate	η^a [mV]	Tafel slope [mV/dec]	Ref.
M-PCBN	1 M KOH	Carbon cloth	232	32	This work
		Cu foam	185		
		Glassy carbon electrode	266		
Co ₃ O ₄ C-NA	0.1 M KOH	Cu foil	290	70	S1
Single-unit-cell CoSe ₂ sheet	1 M KOH	Glassy carbon electrode	270	64	S2
Co ₃ O ₄ nanosheet	1 M KOH	Carbon paper	270	46	S3
NiCo-UMOFNs	1 M KOH	Glassy carbon electrode	250	42	S4
		Cu foam	189		
(Ni ₁ Co) _{0.85} Se@NiCo-LDH	1 M KOH	Carbon cloth	216	77	S5
CoFe ₂ O ₄ /C NRAs	1 M KOH	Ni foam	220	45	S6
Fe ₃ -Co ₂ @GC	0.1 M KOH	Glassy carbon electrode	255	43	S7
NiFe-MOF array	0.1 M KOH	Ni foam	240	34	S8
NiFe LDH-NS@DG10	1 M KOH	Glassy carbon electrode	210	52	S9
CoFe LDHs-Ar	1 M KOH	Glassy carbon electrode	266	38	S10
CS-NiFeCu	1 M KOH	Ni foam	180	33	S11
Ni-Fe LDH hollow prisms	1 M KOH	Glassy carbon electrode	280	49	S12
Au/NiFe LDH	1 M KOH	Ti mesh	237	36	S13
FeOOH _{2nm} /LDH	1 M KOH	Glassy carbon electrode	174	27	S14
O-Co ₃ O ₄	1 M KOH	Ni foam	220	49	S15
Fe-Co-P	1 M KOH	Glassy carbon electrode	252	33	S16
CoFeZr oxides/NF	1 M KOH	Ni foam	248	54	S17
NiCoFe@NiCoFeO NTAs/CFC	1 M KOH	Carbon cloth	201	39	S18
Co@N-CS/N-HCP@CC	1 M KOH	Carbon cloth	248	68	S19
Co ₃ S ₄ /EC-MOF	1 M KOH	Carbon cloth	226	132	S20
CoBDC-Fc-NF	1 M KOH	Ni foam	178	51	S21

^aThe overpotential η was measured at the current density of 10 mA/cm².

References

- S1 Ma, T. Y.; Dai, S.; Jaroniec, M.; Qiao, S. Z. Metal-Organic Framework Derived Hybrid Co_3O_4 -Carbon Porous Nanowire Arrays as Reversible Oxygen Evolution Electrodes. *J. Am. Chem. Soc.* **2014**, *136*, 13925—13931.
- S2 Liang, L.; Cheng, H.; Lei, F.; Han, J.; Gao, S.; Wang, W.; Sun, Y.; Qamar, S.; Wei, S.; Xie, Y. Metallic Single-Unit-Cell Orthorhombic Cobalt Diselenide Atomic Layers: Robust Water-Electrolysis Catalysts. *Angew. Chem. Int. Ed.* **2015**, *54*, 12004—12008.
- S3 Dai, L.; Qin, Q.; Zhao, X.; Xu, C.; Hu, C.; Mo, S.; Wang, Y. O.; Lin, S.; Tang, Z.; Zheng, N. Electrochemical Partial Reforming of Ethanol into Ethyl Acetate Using Ultrathin Co_3O_4 Nanosheets as a Highly Selective Anode Catalyst. *ACS Cent. Sci.* **2016**, *2*, 538—544.
- S4 Zhao, S.; Wang, Y.; Dong, J.; He, C.-T.; Yin, H.; An, P.; Zhao, K.; Zhang, X.; Gao, C.; Zhang, L.; Lv, J.; Wang, J.; Zhang, J.; Khattak, A. M.; Khan, N. A.; Wei, Z.; Zhang, J.; Liu, S.; Zhao, H.; Tang, Z. Ultrathin Metal-Organic Framework Nanosheets for Electrocatalytic Oxygen Evolution. *Nat. Energy* **2016**, *1*, 16184.
- S5 Xia, C.; Jiang, Q.; Zhao, C.; Hedhili, M. N.; Alshareef, H. N. Selenide-Based Electrocatalysts and Scaffolds for Water Oxidation Applications. *Adv. Mater.* **2016**, *28*, 77—85.
- S6 Lu, X.-F.; Gu, L.-F.; Wang, J.-W.; Wu, J.-X.; Liao, P.-Q.; Li, G.-R. Bimetal-Organic Framework Derived $\text{CoFe}_2\text{O}_4/\text{C}$ Porous Hybrid Nanorod Arrays as High-Performance Electrocatalysts for Oxygen Evolution Reaction. *Adv. Mater.* **2017**, *29*, 1604437.
- S7 Shen, J.-Q.; Liao, P.-Q.; Zhou, D.-D.; He, C.-T.; Wu, J.-X.; Zhang, W.-X.; Zhang, J.-P.; Chen, X.-M. Modular and Stepwise Synthesis of a Hybrid Metal-Organic Framework for Efficient Electrocatalytic Oxygen Evolution. *J. Am. Chem. Soc.* **2017**, *139*, 1778—1781.
- S8 Duan, J.; Chen, S.; Zhao, C. Ultrathin Metal-Organic Framework Array for Efficient Electrocatalytic Water Splitting. *Nat. Commun.* **2017**, *8*, 15341.
- S9 Jia, Y.; Zhang, L.; Gao, G.; Chen, H.; Wang, B.; Zhou, J.; Soo, M. T.; Hong, M.; Yan, X.; Qian, G.; Zou, J.; Du, A.; Yao, X. A Heterostructure Coupling of Exfoliated Ni-Fe Hydroxide Nanosheet and Defective Graphene as a Bifunctional Electrocatalyst for Overall Water Splitting. *Adv. Mater.* **2017**, *29*, 1700017.
- S10 Wang, Y.; Zhang, Y.; Liu, Z.; Xie, C.; Feng, S.; Liu, D.; Shao, M.; Wang, S. Layered Double Hydroxide Nanosheets with Multiple Vacancies Obtained by Dry Exfoliation as Highly Efficient Oxygen Evolution Electrocatalysts. *Angew. Chem. Int. Ed.* **2017**, *56*, 5867—5871.
- S11 Zhang, P.; Li, L.; Nordlund, D.; Chen, H.; Fan, L.; Zhang, B.; Sheng, X.; Daniel, Q.; Sun, L. Dendritic Core-Shell Nickel-Iron-Copper Metal/Metal Oxide Electrode for Efficient Electrocatalytic Water Oxidation. *Nat. Commun.* **2018**, *9*, 381.
- S12 Yu, L.; Yang, J. F.; Guan, B. Y.; Lu, Y.; Lou, X. W. Hierarchical Hollow Nanoprisms Based on Ultrathin Ni-Fe Layered Double Hydroxide Nanosheets with Enhanced Electrocatalytic Activity towards Oxygen Evolution. *Angew. Chem. Int. Ed.* **2018**, *57*, 172—176.
- S13 Zhang, J.; Liu, J.; Xi, L.; Yu, Y.; Chen, N.; Sun, S.; Wang, W.; Lange, K. M.; Zhang, B. Single-Atom Au/NiFe Layered Double Hydroxide Electrocatalyst: Probing the Origin of Activity for Oxygen Evolution Reaction. *J. Am. Chem. Soc.* **2018**, *140*, 3876—3879.
- S14 Chen, J.; Zheng, F.; Zhang, S.-J.; Fisher, A.; Zhou, Y.; Wang, Z.; Li, Y.; Xu, B.-B.; Li, J.-T.; Sun, S.-G. Interfacial Interaction between FeOOH and Ni-Fe LDH to Modulate the Local Electronic Structure for Enhanced OER Electrocatalysis. *ACS Catal.* **2018**, *8*, 11342—11351.

- S15 Cai, Z.; Bi, Y.; Hu, E.; Liu, W.; Dwarica, N.; Tian, Y.; Li, X.; Kuang, Y.; Li, Y.; Yang, X.-Q.; Wang, H.; Sun, X. Single-Crystalline Ultrathin Co_3O_4 Nanosheets with Massive Vacancy Defects for Enhanced Electrocatalysis. *Adv. Energy Mater.* **2018**, *8*, 1701694.
- S16 Liu, K.; Zhang, C.; Sun, Y.; Zhang, G.; Shen, X.; Zou, F.; Zhang, H.; Wu, Z.; Wegener, E. C. Taubert, C. J.; Miller J. T.; Peng, Z.; Zhu, Y. High-Performance Transition Metal Phosphide Alloy Catalyst for Oxygen Evolution Reaction. *ACS Nano* **2018**, *12*, 158—167.
- S17 Huang, L.; Chen, D.; Luo, G.; Lu, Y.-R.; Chen, C.; Zou, Y.; Dong, C.-L.; Li, Y.; Wang, S. Zirconium-Regulation-Induced Bifunctionality in 3D Cobalt–Iron Oxide Nanosheets for Overall Water Splitting. *Adv. Mater.* **2019**, *31*, 1901439.
- S18 Liu, Y.; Ying, Y.; Fei, L.; Liu, Y.; Hu, Q.; Zhang, G.; Pang, S. Y.; Lu, W.; Mak, C. L.; Luo, X. Valence Engineering *via* Selective Atomic Substitution on Tetrahedral Sites in Spinel Oxide for Highly Enhanced Oxygen Evolution Catalysis. *J. Am. Chem. Soc.* **2019**, *141*, 8136—8145.
- S19 Chen, Z.; Ha, Y.; Jia, H.; Yan, X.; Chen, M.; Liu, M.; Wu, R. Oriented Transformation of Co-LDH into 2D/3D ZIF-67 to Achieve Co–N–C Hybrids for Efficient Overall Water Splitting. *Adv. Energy Mater.* **2019**, *9*, 1803918.
- S20 Liu, T.; Li, P.; Yao, N.; Kong, T.; Cheng, G.; Chen, S.; Luo, W. Self-Sacrificial Template-Directed Vapor-Phase Growth of MOF Assemblies and Surface Vulcanization for Efficient Water Splitting. *Adv. Mater.* **2019**, *31*, 1806672.
- S21 Xue, Z.; Liu, K.; Liu, Q.; Li, Y.; Li, M.; Su, C.-Y.; Ogiwara, N.; Kobayashi, H.; Kitagawa, H.; Liu, M.; Li, G. Missing-Linker Metal–Organic Frameworks for Oxygen Evolution Reaction. *Nat. Commun.* **2019**, *10*, 5048.